Received: 15 November 2018 | Revised: 24 April 2019 | Accepted: 18 May 2019

DOI: 10.1002/nag.2987

RESEARCH ARTICLE

WILEY

Transient analysis of full-space unbounded domains by reciprocal absorbing boundaries

Cuong T. Nguyen[1] | **John L. Tassoulas**[2]

[1]Department of Computational Engineering, Vietnamese-German University, Vietnam

[2]Department of Civil, Architectural and Environmental Engineering, The University of Texas at Austin, Austin, Texas, U.S.A

Correspondence
Cuong T. Nguyen, Le Lai Street, Thu Dau Mot City, Binh Duong, Vietnam.
Email: cuong.nt@vgu.edu.vn

John L. Tassoulas, 301 E. Dean Keeton St. Stop C1700, Austin, Texas 78712-0273, U.S.A.
Email: yannis@mail.utexas.edu

Summary

In this paper, we explore a combination of the reciprocal absorbing boundary condition with perfectly matched discrete layers for the time-domain analysis of wave motion in the full plane. Coupling of these absorbing boundaries leads to solutions for out-of-plane as well as in-plane excitations of the full plane. Together with numerical transient simulations, harmonic analysis is also carried out for the purpose of verifying the results by comparing with available exact frequency-domain solutions. The proposed combination is investigated through several numerical examples, which demonstrate its accuracy and efficiency.

KEYWORDS

absorbing boundary conditions, full-space unbounded domains, reciprocity theorems, perfectly matched discrete layers, wave propagation

1 | INTRODUCTION

Problems of wave propagation are often formulated in unbounded domains. This is the case in seismology, geophysical exploration, earthquake engineering, dynamic soil-structure interaction, geotechnical site characterization, and nondestructive evaluation, to mention a few areas of current research interest. Typically, in such problems, the analyst is most concerned with the response of the so-called *near field*, for example, in dynamic soil-structure interaction, the soil in a neighborhood of a structural foundation. Normally, the near field encompasses most or all irregularities and material or other nonlinearities. On the other hand, the rest of the domain, the *far field*, performs in the linear range. It is then desirable or imperative to represent the far field as efficiently and accurately as possible in terms of its dynamic characteristics stemming from inertia, dissipative behavior, and stiffness of the unbounded medium.

In all developments to date, the approach has been to apply conditions on the boundary of a computational domain that contains the near field. These conditions are intended to describe, to various degrees of accuracy, the effects of the far field on the near field. Collectively, they are referred to as absorbing boundary conditions ("ABCs," also known as "transmitting" or "nonreflecting") since the primary objective is to "absorb" or allow outward traveling incident waves. There have been developments of "local" and "global or nonlocal" ABCs in the frequency and time domains. Examples of nonlocal ABCs are those based on the boundary integral equation method where Green's functions for the infinite domain are used along with reciprocity equations to obtain a representation, in the frequency or time domains, of the far field that involves the *entire* absorbing boundary (see the report by Brebbia and Dominguez[1] and the review by Tassoulas[2]). Another nonlocal development in the frequency domain has been the synthesis of a transmitting boundary in terms of wave modes derived for horizontally layered media by the finite element method. The latter contribution is due to Waas[3] and Kausel.[4]

Local ABCs have been based on approximations of the one-way wave equation in frequency-wavenumber space. The lowest-order approximation involves a single boundary point and is particularly easy to implement and apply. However, such simple ABCs have been shown to require a rather extensive computational domain. Otherwise, waves would

be reflected by the boundary and return to produce spurious response in the near field. The quality of local ABCs was improved by the introduction of hierarchies of high-order ABCs. Examples include the families of ABCs developed by Engquist and Majda[5] and Higdon.[6] While high-order local ABCs perform well (see Kausel and Tassoulas[7]), the implementation in numerical frameworks such as the finite element method is quite challenging. Guddati and Tassoulas[8] presented a procedure based on continued fractions for efficient implementation of arbitrarily-high-order local ABCs.

Perhaps, the most versatile realization of local ABCs has been the introduction of "perfectly matched layers" (PMLs) that provide smooth conversion (ie, without reflection) of traveling waves to evanescent ones upon incidence on the boundary. The energy carried by the incident waves is expended in the PMLs and (ideally) does not return to the near field. A relatively crude version of this dissipative ABC had been introduced by Israeli and Orszag[9] in the form of "sponge layers" while the elegant formulation of PMLs was pioneered by Berenger.[10] In a related development, Guddati and Lim[11] have shown how perfectly matched *discrete* layers (PMDLs) can be incorporated directly and seamlessly in finite element analysis. Also notable is the early work by Basu and Chopra[12] in which the use of PMLs with elastic waves was explored. Although the PMLs are successful with regard to numerical accuracy, this absorbing condition still faces the main challenge, which is the unstability in long-time simulation. In order to resolve this drawback, Meza-Fajardo and Papageorgiou[21] proposed the multiaxial PML (M-PML), which is based on a nonconvolutional formulation and a specification of damping profiles of PML in several directions. The M-PML approach led to stability improvements in comparison with conventional PML, not only in isotropic but also in anisotropic media.

Exploiting the dissipative nature of unbounded domains, other absorbing boundaries have been proposed. For example, Semblat et al[22] applied appropriate Rayleigh/Caughey damping coefficients to attenuate the spurious reflections on the artificial boundary. This approach, therefore, has been referred to as a Caughey absorbing layer method (CALM). In the same vein, Liu and Jerry[23] proposed the ALID method by attaching absorbing layers with increased damping coefficients on the boundary of the near-field. These approaches are very convenient since the damping matrix can be computed easily and is often available in commercial finite-element packages.

Recently, the authors have introduced a novel nonlocal condition by means of reciprocity equations (reciprocal ABCs [RABCs]). Unlike earlier developments, the RABCs do not require availability of Green's functions for the unbounded domain. In fact, Green's functions are obtained as a by-product of RABCs. The conditions take advantage of the fact that reciprocity holds between infinite domains that differ only by the boundary location. For example, if the infinite domain is a layered medium with free surface and fixed base (layered stratum), the domains extending outward of any vertical boundary are identical and, therefore, candidates for application of reciprocity equations. In a series of articles,[13-15 & 24] the authors have described RABCs for layered strata and half-space, elastic, and scalar waves. In the present paper, an extension of RABCs to a full space, in particular, a full plane, is presented. We show how RABCs can be combined with PMDLs to treat the unbounded region exterior to a circular disk undergoing axial (out-of-plane), radial, torsional, and lateral (in-plane) vibrations. Computational results are presented and compared with exact solutions and numerical ones from extended finite-element meshes.

2 | RECIPROCAL ABSORBING BOUNDARY CONDITION

2.1 | Acceleration-based reciprocity theorem

The reciprocity theorem in terms of displacements[16] for the same body in two elastodynamic states I and E can be written as

$$\int_\Gamma t_j^I(\mathbf{x},t) * u_j^E(\mathbf{x},t)d\Gamma + \int_R f_j^I(\mathbf{x},t) * u_j^E(\mathbf{x},t)dR + \rho\int_R \left[u_j^I(\mathbf{x},0^+)v_j^E(\mathbf{x},t) + v_j^I(\mathbf{x},0^+)u_j^E(\mathbf{x},t)\right]dR$$
$$= \int_\Gamma t_j^E(\mathbf{x},t) * u_j^I(\mathbf{x},t)d\Gamma + \int_R f_j^E(\mathbf{x},t) * u_j^I(\mathbf{x},t)dR + \rho\int_R \left[u_j^E(\mathbf{x},0^+)v_j^I(\mathbf{x},t) + v_j^E(\mathbf{x},0^+)u_j^I(\mathbf{x},t)\right]dR, \quad (1)$$

where u_j, v_j, t_j, and f_j are, respectively, displacements, velocities, tractions, and body forces in the two states, while ρ is the mass density. An asterisk denotes a convolution integral, defined as

$$t_j^I(\mathbf{x},t) * u_j^E(\mathbf{x},t) = \int_0^t t_j^I(\mathbf{x},t-\tau)u_j^E(\mathbf{x},\tau)d\tau. \quad (2)$$

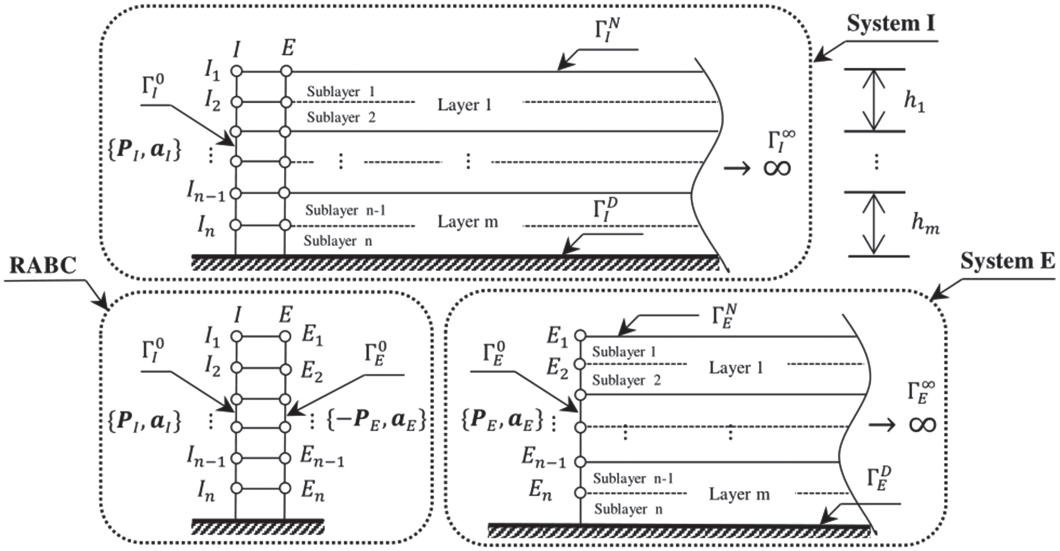

FIGURE 1 The reciprocal absorbing boundary condition

As shown in Section 2 of Nguyen and Tassoulas,[14] the reciprocity theorem can be written in an alternative form involving accelerations and tractions as follows:

$$\int_{\Gamma_I} \tau_j^I(\mathbf{x},t) * a_j^E(\mathbf{x},t)d\Gamma = \int_{\Gamma_E} \tau_j^E(\mathbf{x},t) * a_j^I(\mathbf{x},t)d\Gamma. \tag{3}$$

The latter form is not only equivalent but preferable in many practical applications of interest with silent initial conditions. Let us consider the problem of a stratum as depicted in Figure 1, the boundary conditions on the surface, the base (bedrock), and the infinite boundary toward the right allow us to reduce the integrals in Equation (14) to ones involving only the near-field boundaries Γ_I^0 and Γ_E^0:

$$\int_{\Gamma_I^0} \tau_j^I(\mathbf{x},t) * a_j^E(\mathbf{x},t)d\Gamma = \int_{\Gamma_E^0} \tau_j^E(\mathbf{x},t) * a_j^I(\mathbf{x},t)d\Gamma. \tag{4}$$

Within the finite-element framework, the region between the two boundaries Γ_I^0 and Γ_E^0 is vertically discretized by sufficiently small elements as in Figure 1. Such a discretization builds a column of elements, and the discrete version of Equation (4) for this column can be expressed as

$$\mathbf{P}_I^T(t) * \mathbf{a}_E(t) = \mathbf{P}_E^T(t) * \mathbf{a}_I(t), \tag{5}$$

where $\mathbf{P}_I(t), \mathbf{a}_I(t)$ and $\mathbf{P}_E(t), \mathbf{a}_E(t)$ are force and acceleration vectors on Γ_I^0 and Γ_E^0, respectively.

2.2 | The construction of RABC

In order to obtain the RABC,[13] we solve n problems, simultaneously, where n is the number of degrees of freedom on the boundary Γ_I^0. Specifically, in each problem, an unit-step force is applied on this boundary. Using the trapezoidal rule[13] and applying the reciprocity equation (Equation 5) between the jth and the lth problems leads to

$$\mathbf{P}_{El}^{(1)} \cdot \mathbf{a}_{Ij}^{(k+1)} - \mathbf{P}_{Ij}^{(1)} \cdot \mathbf{a}_{El}^{(k+1)} + \mathbf{a}_{Ij}^{(1)} \cdot \mathbf{P}_{El}^{(k+1)} = \mathbf{P}_{Ij}^{(k+1)} \cdot \mathbf{a}_{El}^{(1)} + C_{jl}^{(k)} - C_{lj}^{(k)}, \tag{6}$$

where Cs are calculated as

$$C_{jl}^{(k)} = 2\sum_{m=2}^{k} \mathbf{P}_{Ij}^{(k+2-m)} \cdot \mathbf{a}_{El}^{(m)}, \tag{7}$$

$$C_{lj}^{(k)} = 2\sum_{m=2}^{k} \mathbf{P}_{El}^{(k+2-m)} \cdot \mathbf{a}_{Ij}^{(m)}. \tag{8}$$

Now, it is time to use the equilibrium equations of the column in RABC. In particular, the equation for the jth problem is given by

$$\left[\begin{array}{c|c} \underset{2n\times 2n}{\left[\widehat{\mathbf{M}}\right]} & \begin{matrix}\mathbf{0}\\ n\times n\end{matrix} \\ & \begin{matrix}\mathbf{I}\\ n\times n\end{matrix} \end{array}\right] \left\{\begin{array}{c} \mathbf{a}_{Ij} \\ \mathbf{a}_{Ej} \\ \widehat{\mathbf{P}}_{Ej} \end{array}\right\}^{(k+1)} = \left\{\begin{array}{c} \widehat{\mathbf{P}}_{Ij} \\ \mathbf{0} \end{array}\right\}^{(k+1)}. \tag{9}$$

We have adopted here the Newmark method[17] for solving the semidiscrete equation of motion, which is expressed as

$$\mathbf{M}\mathbf{a}_{k+1} + \mathbf{C}\mathbf{v}_{k+1} + \mathbf{K}\mathbf{u}_{k+1} = \mathbf{P}_{k+1} \quad \text{at } t_{k+1}. \tag{10}$$

The matrix $\widehat{\mathbf{M}}$ and the vector $\widehat{\mathbf{P}}_{k+1}$ are given by

$$\widehat{\mathbf{M}} = \mathbf{M} + \gamma\Delta t\mathbf{C} + \beta\Delta t^2\mathbf{K}, \tag{11}$$

$$\widehat{\mathbf{P}}_{k+1} = \mathbf{P}_{k+1} - \mathbf{C}\left[\mathbf{v}_k + (1-\gamma)\Delta t\mathbf{a}_k\right] - \mathbf{K}\left[\mathbf{u}_k + \Delta t\mathbf{v}_k + (0.5-\beta)\Delta t^2\mathbf{a}_k\right], \tag{12}$$

where $\beta = 1/4$ and $\gamma = 1/2$ are two basic coefficients of the average-acceleration version of the Newmark method.

So far, we have obtained $3n^2$ equations consisting of $2n^2$ equilibrium equations (Equation 9) and n^2 reciprocity equations (Equation 6). Therefore, it is straightforward to solve for $3n^2$ unknowns including $\mathbf{a}_{Ij}^{(k+1)}$, $\mathbf{a}_{Ej}^{(k+1)}$, and $\widehat{\mathbf{P}}_{Ej}^{(k+1)}$. Finally, once $\mathbf{a}_{Ij}^{(k+1)}$ and $\mathbf{a}_{Ej}^{(k+1)}$ are computed, $\mathbf{u}_{Ij}^{(k+1)}$, $\mathbf{u}_{Ej}^{(k+1)}$ and $\mathbf{v}_{Ij}^{(k+1)}$, $\mathbf{v}_{Ej}^{(k+1)}$ can be updated by the Newmark method as follows:

$$\mathbf{u}_{k+1} = \mathbf{u}_k + \Delta t\mathbf{v}_k + \Delta t^2\left[(0.5-\beta)\mathbf{a}_k + \beta\mathbf{a}_{k+1}\right], \tag{13}$$

$$\mathbf{v}_{k+1} = \mathbf{v}_k + \Delta t\left[(1-\gamma)\mathbf{a}_k + \gamma\mathbf{a}_{k+1}\right]. \tag{14}$$

3 | PERFECTLY MATCHED DISCRETE LAYERS

3.1 | Semidiscrete equation of motion

3.1.1 | Anti-plane shear

Following the procedure described in Guddati and Lim,[11] in the last step of implementing PMDLs, we couple edge absorbing elements to the interior domain. This coupling yields the global system of governing equations in time

$$\mathbf{M}_i\mathbf{U}_{tt} + \mathbf{C}_e\mathbf{U}_t + \mathbf{K}_i\mathbf{U} + \mathbf{R}_e\int_0^t \mathbf{U}d\tau = \mathbf{P}_i, \tag{15}$$

where $\mathbf{P}_i$ is the load vector resulting from the interior. $\mathbf{M}_i$ and $\mathbf{K}_i$ are respectively the mass and stiffness matrices of the interior domain. The subscripts i, e here stand for interior and edge absorbing elements, respectively.

Two other matrices $\mathbf{C}_e$ and $\mathbf{R}_e$ on the left-hand side are assembled from PMDL-edge elements as the following:

$$\mathbf{C}_e = \sum_{n=1}^{N_{\text{pmdl}}} \mathbf{C}_e^j, \tag{16}$$

$$\mathbf{R}_e = \sum_{n=1}^{N_{\text{pmdl}}} \mathbf{R}_e^j, \tag{17}$$

where N_{pmdl} is the number of PMDL-edge elements, and for each element,

$$\mathbf{C}_e^j = \int_{\Gamma_j} \mathbf{N}_\Gamma^T\mathbf{C}^j\mathbf{N}_\Gamma dx, \tag{18}$$

$$\mathbf{R}_e^j = \int_{\Gamma_j} \frac{\partial \mathbf{N}_\Gamma^T}{\partial x} \mathbf{R}^j \frac{\partial \mathbf{N}_\Gamma}{\partial x} dx. \tag{19}$$

In the above equations, the matrix of shape functions $\mathbf{N}_\Gamma$ is defined as

$$\mathbf{N}_\Gamma = \begin{bmatrix} N_1 & 0 & \dots & N_k & 0 \\ 0 & N_1 & \dots & 0 & N_k \end{bmatrix}, \tag{20}$$

in which k is the number of boundary nodes in the x-direction. Matrices $\mathbf{C}^j$ and $\mathbf{R}^j$ in the integrands are computed as

$$\mathbf{C}^j = \frac{\mu}{2c_j} \begin{bmatrix} +1 & -1 \\ -1 & +1 \end{bmatrix} + \frac{\rho c_j}{2} \begin{bmatrix} 1 & 1 \\ 1 & 1 \end{bmatrix}, \tag{21}$$

$$\mathbf{R}^j = \frac{\mu c_j}{2} \begin{bmatrix} 1 & 1 \\ 1 & 1 \end{bmatrix}. \tag{22}$$

The shear modulus is denoted by μ, while c^j denotes the reference phase velocity of the jth PMDL-edge element:

$$c_j = \frac{c_s}{\cos\left[\frac{\pi(j-1)}{2n}\right]}, \quad n = 5, \tag{23}$$

where $c_s = \sqrt{\mu/\rho}$ is the shear-wave speed. This choice of the reference phase velocity is based on minimizing the reflection coefficient due to truncating PMDL elements, ie, applying the fixed boundary at the bottom of n PMD layers.

3.1.2 | Plane strain

In plane strain,[18] coupling edge elements to the interior domain again gives us a *third-order* differential equation in time,

$$\mathbf{M}_i \mathbf{U}_{tt} + \mathbf{C}_e \mathbf{U}_t + (\mathbf{K}_i + \mathbf{K}_e)\,\mathbf{U} + \mathbf{R}_e \int_0^t \mathbf{U} d\tau = \mathbf{P}_i, \tag{24}$$

where $\mathbf{P}_i$ is the resultant force from the interior. The semidiscrete equation here is slightly different from Equation (15) since it has an additional term $\mathbf{K}_e$. On the left-hand side, the matrices $\mathbf{C}_e$, $\mathbf{K}_e$, and $\mathbf{R}_e$ are computed by assembling element matrices:

$$\mathbf{C}_e^j = \int_{-1}^{1}\int_{-1}^{1} \left(\frac{l_x}{2c_j} \mathbf{B}_{\eta\eta}^T \mathbf{D}_{\eta\eta} \mathbf{B}_{\eta\eta} + \frac{l_x c_j \rho}{2} \mathbf{N}^T \mathbf{N} \right) d\xi d\eta + \int_{-1}^{1}\int_{-1}^{1} \left(\mathbf{B}_{\xi\eta}^T \mathbf{D}_{\xi\eta} \mathbf{B}_{\xi\eta} + \mathbf{B}_{\eta\xi}^T \mathbf{D}_{\eta\xi} \mathbf{B}_{\eta\xi} \right) d\xi d\eta, \tag{25}$$

$$\mathbf{K}_e^j = \int_{-1}^{1}\int_{-1}^{1} \left(\mathbf{B}_{\xi\eta}^T \mathbf{D}_{\xi\eta} \mathbf{B}_{\xi\eta} + \mathbf{B}_{\eta\xi}^T \mathbf{D}_{\eta\xi} \mathbf{B}_{\eta\xi} \right) d\xi d\eta, \tag{26}$$

$$\mathbf{R}_e^j = \int_{-1}^{1}\int_{-1}^{1} \frac{2c_j}{l_x} \mathbf{B}_{\eta\eta}^T \mathbf{D}_{\eta\eta} \mathbf{B}_{\eta\eta} d\xi d\eta, \tag{27}$$

where

$$\mathbf{B}_{\eta\eta} = \begin{bmatrix} \frac{\partial N_1}{\partial \eta} & 0 & \frac{\partial N_2}{\partial \eta} & 0 & \frac{\partial N_3}{\partial \eta} & 0 & \frac{\partial N_4}{\partial \eta} & 0 \\ 0 & \frac{\partial N_1}{\partial \eta} & 0 & \frac{\partial N_2}{\partial \eta} & 0 & \frac{\partial N_3}{\partial \eta} & 0 & \frac{\partial N_4}{\partial \eta} \end{bmatrix}, \tag{28}$$

$$\mathbf{B}_{\eta\xi} = \begin{bmatrix} \frac{\partial N_1}{\partial \eta} & 0 & \frac{\partial N_2}{\partial \eta} & 0 & \frac{\partial N_3}{\partial \eta} & 0 & \frac{\partial N_4}{\partial \eta} & 0 \\ 0 & \frac{\partial N_1}{\partial \xi} & 0 & \frac{\partial N_2}{\partial \xi} & 0 & \frac{\partial N_3}{\partial \xi} & 0 & \frac{\partial N_4}{\partial \xi} \end{bmatrix}, \tag{29}$$

$$\mathbf{B}_{\xi\eta} = \begin{bmatrix} \frac{\partial N_1}{\partial \xi} & 0 & \frac{\partial N_2}{\partial \xi} & 0 & \frac{\partial N_3}{\partial \xi} & 0 & \frac{\partial N_4}{\partial \xi} & 0 \\ 0 & \frac{\partial N_1}{\partial \eta} & 0 & \frac{\partial N_2}{\partial \eta} & 0 & \frac{\partial N_3}{\partial \eta} & 0 & \frac{\partial N_4}{\partial \eta} \end{bmatrix}, \tag{30}$$

$$\mathbf{D}_{\eta\eta} = \begin{bmatrix} \mu & 0 \\ 0 & \lambda + 2\mu \end{bmatrix}, \ \mathbf{D}_{\xi\eta} = \begin{bmatrix} 0 & \lambda \\ \lambda & 0 \end{bmatrix}, \ \mathbf{D}_{\eta\xi} = \begin{bmatrix} 0 & \mu \\ \mu & 0 \end{bmatrix}, \tag{31}$$

and $\mathbf{N}$ is the matrix of shape functions,

$$\mathbf{N} = \begin{bmatrix} N_1 & 0 & N_2 & 0 & N_3 & 0 & N_4 & 0 \\ 0 & N_1 & 0 & N_2 & 0 & N_3 & 0 & N_4 \end{bmatrix}, \tag{32}$$

with λ, μ being Lamé constants and N_is are the shape functions of bilinear elements:

$$N_i = \frac{1}{4}(1 - \xi_i\xi)(1 - \eta_i\eta), \quad i = 1, \ldots, 4; \quad \xi \text{ and } \eta \text{ are natural coordinates.} \tag{33}$$

The reference phase velocity in the plane-strain case is calculated using the pressure wave speed as follows:

$$c_j = \frac{c_p}{\cos\left[\frac{\pi(j-1)}{2n}\right]}, \quad n = 5, \tag{34}$$

where $c_p = \sqrt{E/\rho}$, E denotes the elastic modulus.

3.2 | Time-stepping

In both cases, anti-plane shear and plane strain, the global equation of motion can be written in discrete form:

$$\mathbf{M}_i\mathbf{A}_i^{k+1} + \mathbf{K}_i\mathbf{U}_i^{k+1} + \underbrace{\mathbf{K}_e\mathbf{U}_e^{k+1}}_{\text{only in plane-strain case}} + \mathbf{C}_e\mathbf{V}_e^{k+1} + \mathbf{R}_e\mathbf{W}_e^{k+1} = \mathbf{P}^{k+1}. \tag{35}$$

Since the lengths of edge PMDLs are inversely proportional to ω, coupling edge absorbers to the interior domain is conducted by the Crank-Nicolson method:

$$\mathbf{E}^{k+1} = \mathbf{E}^k + \frac{\Delta t}{2}(\mathbf{I}^k + \mathbf{I}^{k+1}), \tag{36}$$

where $\mathbf{E}^k = \left[\mathbf{U}_e^k ; \mathbf{W}_e^k ; \mathbf{V}_e^k\right]$ and $\mathbf{I}^k = \left[\mathbf{V}_i^k ; \mathbf{U}_i^k ; \mathbf{A}_i^k\right]$.

Substituting this expression into the equilibrium equation at time step t_{k+1} (Equation 35), we obtain

$$\mathbf{M}\mathbf{A}_i^{k+1} + \mathbf{K}\mathbf{U}_i^{k+1} = \mathbf{P}^{k+1}, \tag{37}$$

in which

$$\mathbf{M} = \mathbf{M}_i + \frac{\Delta t}{2}\mathbf{C}_e, \tag{38}$$

$$\mathbf{P}^{k+1} = \mathbf{P}_i^{k+1} - \mathbf{C}_e\left(\mathbf{V}_e^k + \frac{\Delta t}{2}\mathbf{A}_i^k\right) - \mathbf{R}_e\left(\mathbf{W}_e^k + \frac{\Delta t}{2}\mathbf{U}_i^k\right). \tag{39}$$

The matrix $\mathbf{K}$ depends on the problem under consideration and is computed as

$$\begin{cases} \mathbf{K} = \mathbf{K}_i + \frac{\Delta t}{2}\mathbf{R}_e & \text{in anti-plane shear,} \\ \mathbf{K} = \mathbf{K}_i + \mathbf{K}_e + \frac{\Delta t}{2}\mathbf{R}_e & \text{in plane strain.} \end{cases} \tag{40}$$

Starting from Equation (37), the Newmark method (Equations 10–14) is applied to advance the solution.

4 | RABC WITH PMDLS

We now consider a semi-infinite system including regular elements and several PMDL-edge elements as shown in Figure 2. As pointed out in Nguyen and Tassoulas,[15] if PMDL-edge elements are treated as regular ones, the

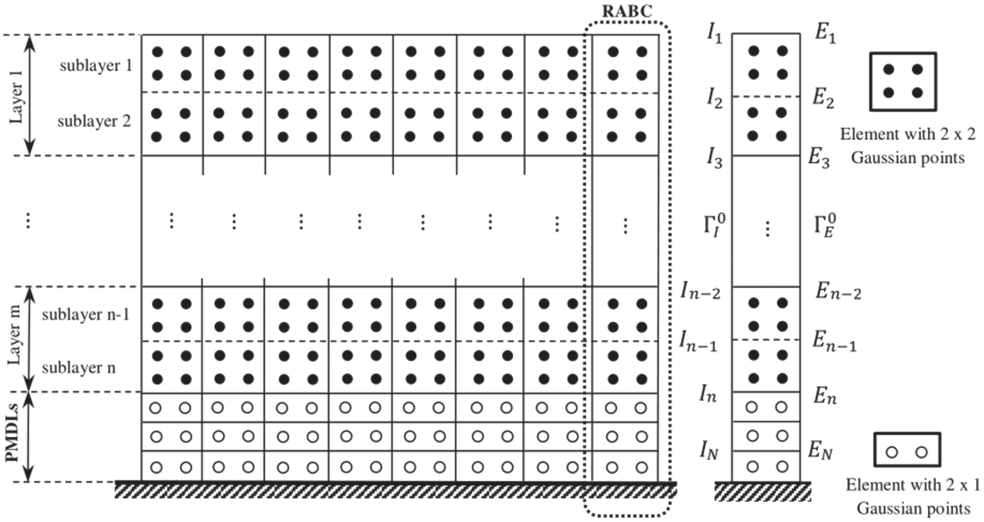

FIGURE 2 Reciprocal absorbing boundary condition (RABC) with perfectly matched discrete layers (PMDLs)

acceleration-based reciprocity equation is still valid. The development of RABCs is thus applicable to the combination of RABCs and PMDLs.

5 | NUMERICAL EXAMPLES

In this section, we present four numerical examples to illustrate the accuracy and effectiveness of combining the RABC with PMDLs for a circle in a full space (full plane), as shown in Figure 3. In each example, we will first apply a transient load and then a harmonic load, both in the time domain, compute the response until a steady state is reached, and, finally, compare with extended-mesh, time-domain calculations, and available exact solutions in the frequency domain, first reported by Baranov[19] and Novak.[20]

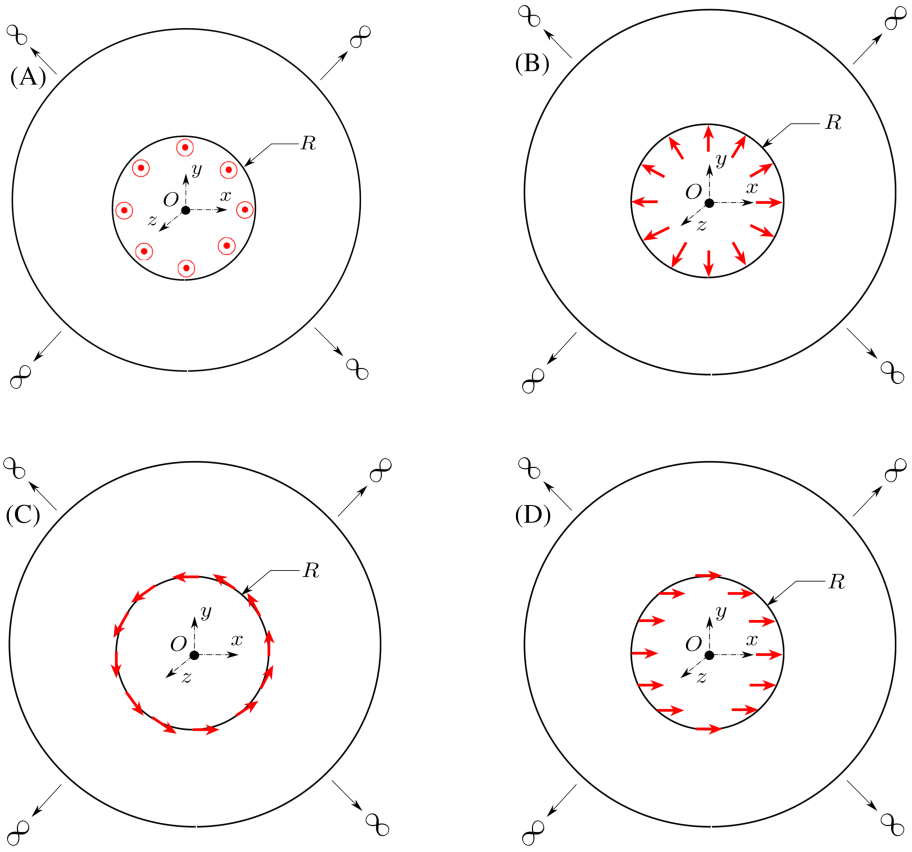

FIGURE 3 A circle of radius R in full space subjected to traction (A) in the vertical (axial) direction, (B) in the radial direction, (C) in the circumferential direction, and (D) in the horizontal (lateral) direction. The material properties of the surrounding full space are taken as $\rho = 1, \mu = 1, \nu = 1/3$. For this set of parameters, the shear and pressure wave speeds are 1 and 2 m/s, respectively [Colour figure can be viewed at wileyonlinelibrary.com]

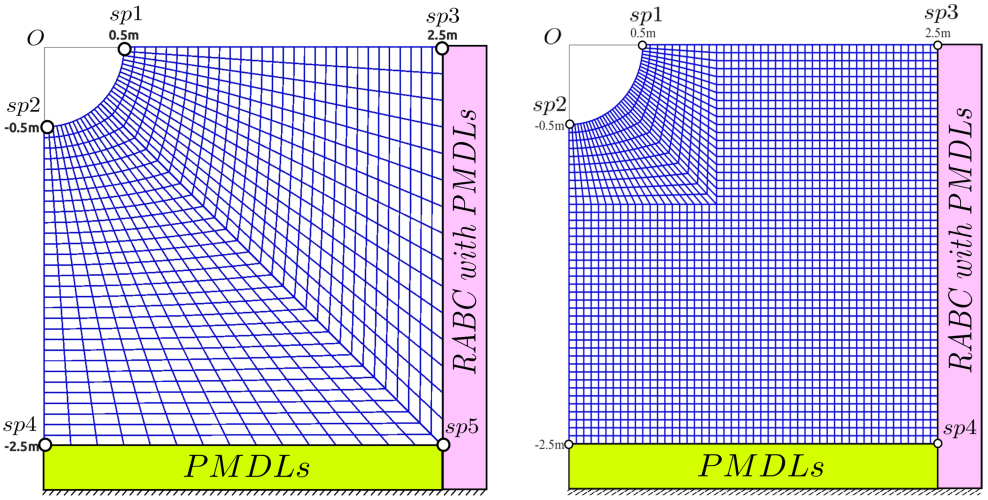

FIGURE 4 Meshes used in computations (the left one is for the vertical and radial cases and the right one is for the torsional and horizontal cases), including perfectly matched discrete layers (PMDLs) on the bottom edge and reciprocal absorbing boundary condition (RABC)-PMDLs on the right edge. Sample points at which the response time history will be plotted below are marked as $sp1, \ldots, sp5$ [Colour figure can be viewed at wileyonlinelibrary.com]

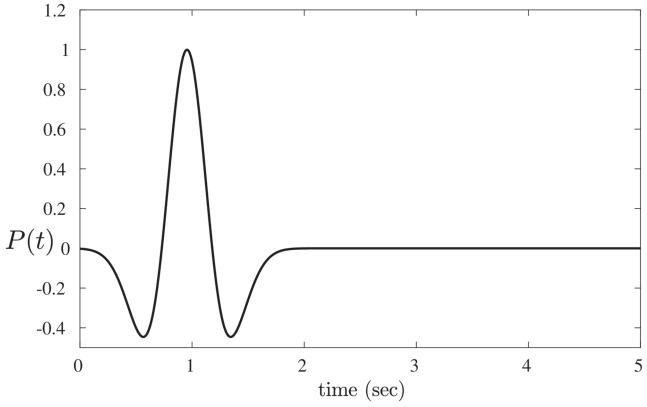

FIGURE 5 Ricker wavelet load with dominant period $t_0 = 1/\pi$ ($t_s = 3t_0 = 3/\pi$)

Because of the (double) symmetry in the four examples, we will analyze only a quarter of the domain. The mesh is depicted in Figure 4, including PMDLs on the bottom edge and RABC-PMDLs on the right edge. This arrangement will be used in all examples. It is worth mentioning that in problems that lack the symmetries of the ones being considered herein, there will be PMDLs-RABC-PMDLs extending to the left as well as to the right.

The transient load on the circle will be taken in the form of a Ricker wavelet as follows:

$$q(t) = a(1 - 2\tau^2)e^{-\tau^2}, \tag{41}$$

where $a = 1$ (amplitude), $\tau = (t - t_s)/t_0$, t_0 is the dominant period of the wavelet), and $t_s = 3t_0$ is the instance when the load reaches its peak), t_0 is taken to be $1/\pi$ in Section 5.1 and $1/(2\pi)$ in Sections 5.2 to 5.4. The Ricker wavelet load for $t_0 = 1/\pi$ is plotted in Figure 5.

5.1 | Vertical (axial) response

First, we consider the vertical response. A uniform traction $q(t)$ is applied in the z-direction. We are interested in computing the time-history of axial displacement $w(t)$.

Figure 6 shows snapshots of the axial wave field at various instances ($t = 1, 1.5, 2, 2.5, 3, 3.5, 4, 4.5, 5$s). We go on to quantitatively examine the accuracy by comparing the solution at selected sample points with those generated using an extended mesh to a distance of 6 m from the circle. By this extended mesh, in the time-interval of interest (up to 5 seconds), since the shear wave speed is c_s =1 m/s, the wave motion of the interior domain is guaranteed to not be affected by any reflections. The time-step size is chosen as $\Delta t = 0.01$ s, and this value is used also in the radial case. For the torsional and horizontal cases, the smaller size of elements requires us to adjust the time-step size. In particular, we use $\Delta t = 0.005$s for these two cases. Figure 7 provides the response (displacement) time histories at sample points $sp1$ and

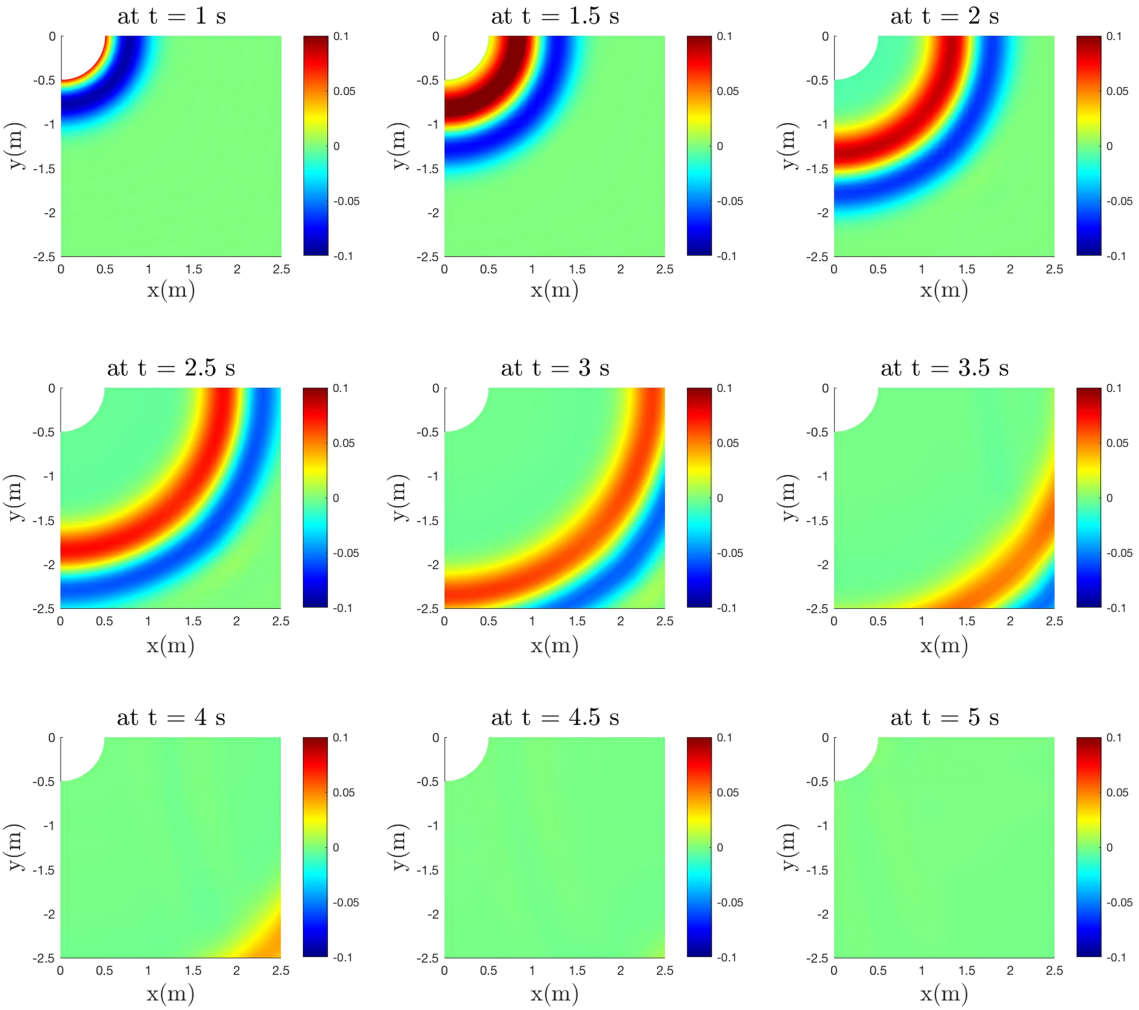

FIGURE 6 Vertical response: Snapshots of the wave field at various instances [Colour figure can be viewed at wileyonlinelibrary.com]

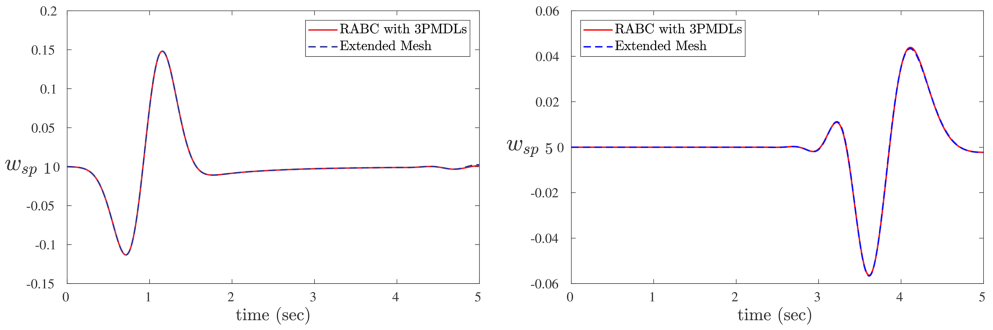

FIGURE 7 Vertical response: Displacement time-histories at sample points [Colour figure can be viewed at wileyonlinelibrary.com]

*sp*5. The performance of the RABC-PMDLs combination is, indeed, excellent. We define the relative error as

$$E = \frac{\|\mathbf{w}^{\text{RABC-PMDLs}}(\mathbf{x}, t) - \mathbf{w}^{\text{ext. mesh}}(\mathbf{x}, t)\|_{L_2}}{\|\mathbf{w}^{\text{ext. mesh}}(\mathbf{x}, t)\|_{L_2}}, \tag{42}$$

where $\mathbf{w}^{\text{RABC-PMDLs}}$ and $\mathbf{w}^{\text{ext. mesh}}$ are respectively solutions obtained by RABC-PMDLs and the extended mesh. Table 1 shows the relative error at each of the sample points. It is clear that the highest error occurs at the point *sp*2 and is about 1.5%, while the error at the point on the circle, *sp*1, is much smaller, (0.5%). At the corner point, *sp*5, normally, the hardest for accuracy, the error is only 1.1%.

TABLE 1 Vertical response: Relative error at sample points between RABC-PMDLs and extended mesh solutions

	w_{sp1}	w_{sp2}	w_{sp3}	w_{sp4}	w_{sp5}
Error	5.3413×10^{-3}	1.5074×10^{-2}	4.7530×10^{-3}	2.5084×10^{-2}	1.1020×10^{-2}

Abbreviations: PMDLs, perfectly matched discrete layers; RABC, reciprocal absorbing boundary condition.

Next, we apply a (unit) harmonic traction

$$q(t) = \cos \omega t \tag{43}$$

and compute the response until a steady state is reached. We, then, extract the amplitude and phase (with respect to the applied traction) of the time-domain response and compare with the frequency-domain results, which are available in closed form. In the case under consideration, we have for the harmonic displacement of the circle:

$$w(a_0) = \frac{1}{S_z(a_0)}, \tag{44}$$

where S_z is the dynamic stiffness given by

$$S_z(a_0) = \frac{\mu a_0}{R} \frac{H_1^{(2)}(a_0)}{H_0^{(2)}(a_0)} = \frac{\mu}{2R} \left[S_{z1}(a_0) + i S_{z2}(a_0) \right], \tag{45}$$

with

$$\begin{cases} S_{z1}(a_0) = 2a_0 \frac{J_0(a_0)J_1(a_0) + Y_0(a_0)Y_1(a_0)}{J_0^2(a_0) + Y_0^2(a_0)}, \\ S_{z2}(a_0) = \frac{4}{\pi \left[J_0^2(\omega_S)^2 + Y_0^2(\omega_S) \right]}. \end{cases} \tag{46}$$

In the above expressions, $a_0 = \omega R / c_s$ is the dimensionless frequency for shear waves. $J_\nu(\cdot)$ and $Y_\nu(\cdot)$ are Bessel functions of the first and second kinds, while $H_\nu^{(2)}(\cdot)$ is the Hankel function of the second kind. The subscripts $\nu = 0, 1$ of these functions denote their orders. The amplitude of the axial displacement on the circle can then be computed as

$$\hat{w}(a_0) = \frac{1}{\frac{\mu}{2R} \sqrt{\left[S_{z1}^2(a_0) + S_{z2}^2(a_0) \right]}}, \tag{47}$$

while the phase of the displacement relative to the traction is given by

$$\phi(a_0) = \tan^{-1} \left[\frac{S_{z2}(a_0)}{S_{z1}(a_0)} \right]. \tag{48}$$

We examine the results obtained by RABC-PMDLs at steady state for three values of the dimensionless frequency $a_0 = 0.1\pi, 0.5\pi, 1.25\pi$. In order to capture the behavior at the high frequency $a_0 = 1.25\pi$, we shrink the interior mesh (see Figure 4) by a factor of 2. We let the solutions reach steady state and compare the amplitudes and phases with the exact frequency-domain solutions. Table 2 summarizes the amplitudes and phases extracted from the time-domain solution at the three frequencies in comparison with the exact frequency-domain results. Again, the agreement is excellent.

5.2 | Radial response

Next, we apply on the circle uniform (radial) pressure $q(t)$. The problem is axisymmetric, so the Dirichlet boundary conditions $v(x, y) = 0$ and $u(x, y) = 0$ are imposed on the edges $y = 0$ and $x = 0$, respectively. First, we view the snapshots of the wave field of the radial displacement (computed as $\sqrt{u^2(\mathbf{x}, t) + v^2(\mathbf{x}, t)}$). Figure 8 provides the snapshots of the radial wave field at $t = 0.8, 1, 1.2, 1.4, 1.6, 3$s when the circle is excited by a Ricker wavelet radial traction with dominant period $t_s = 3/2\pi$. The transient responses at sample points are shown in Figure 9. In this case, the wave speed is $c_p = 2$ m/s. Theoretically, since the point *sp*1 is 2 m from the circle, the wave takes 1 second to arrive at this point. By the same argument, the point *sp*5 remains silent until 1.5 seconds as its distance form the circle is about 3 m. These facts are validated from Figure 9. We proceed to compute the relative errors at sample points. As Table 3 shows, the smallest errors of the radial displacement are about 0.83% and 0.82%, occurring at *sp*1 and *sp*3. The errors at other points satisfy the tolerance normally accepted, all being less than 3%.

TABLE 2 Amplitudes and phases of harmonic responses

Case	Frequency a_0	Amplitudes		Phases	
		RABCs-PMDLs	Exact	RABCs-PMDLs	Exact
Vertical	0.1π	0.9077	0.8990	0.8230	0.8288
	0.5π	0.2960	0.2949	1.2940	1.2889
	1.25π	0.0639	0.0627	1.4489	1.4468
Radial	0.2π	0.3070	0.3110	0.3367	0.3314
	π	0.0891	0.0892	1.5014	1.5028
	1.25π	0.0175	0.0172	1.5355	1.5328
Torsional	0.2π	0.2774	0.2771	0.2213	0.2285
	π	0.1492	0.1471	1.1031	1.1033
	1.25π	0.0309	0.0303	1.1939	1.1934
Horizontal	0.2π	0.4129	0.4135	1.0219	1.0174
	π	0.1025	0.1036	1.4313	1.4341
	1.25π	0.0218	0.0208	1.4569	1.4581

Abbreviations: PMDLs, perfectly matched discrete layers; RABCs, reciprocal absorbing boundary conditions.

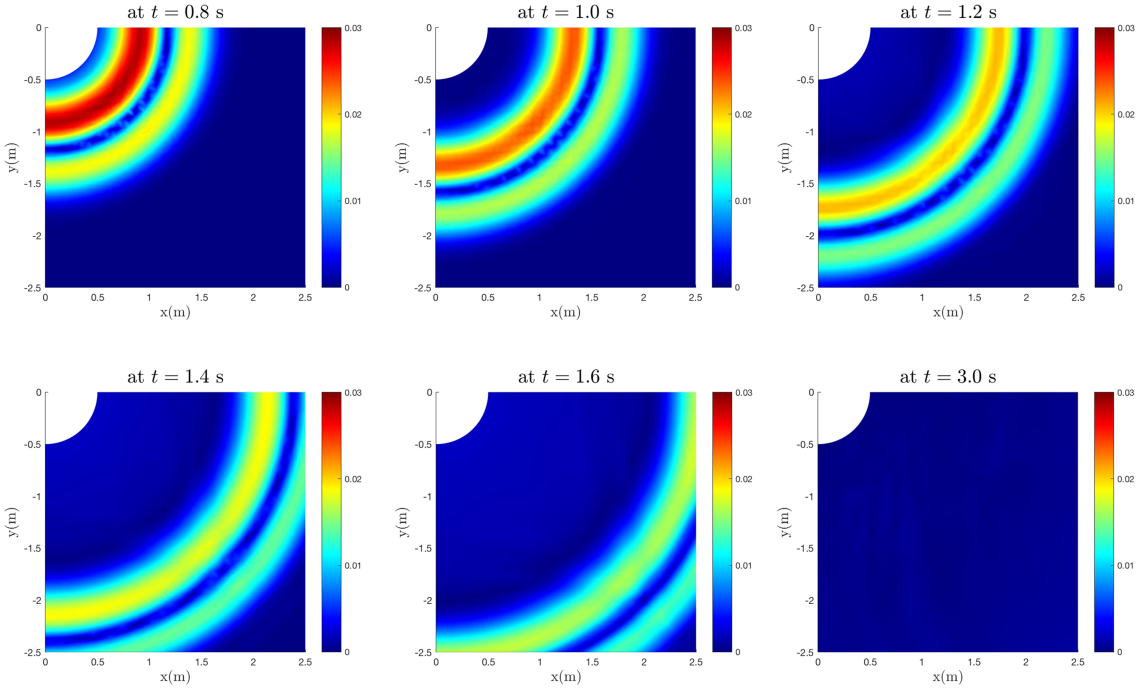

FIGURE 8 Radial response: Snapshots of the wave field of u_r at various times [Colour figure can be viewed at wileyonlinelibrary.com]

The exact harmonic solution for the dynamic radial stiffness is given by

$$S_r(a_p,\eta)=\frac{2\mu}{R}\left[1-\frac{\eta^2 a_p}{2}\frac{H_0^{(2)}(a_p)}{H_1^{(2)}(a_p)}\right]=S_{r1}(a_p,\eta)+iS_{r2}(a_p,\eta), \tag{49}$$

where

$$\begin{cases} S_{r1}(a_p,\eta) = \frac{2\mu}{R}\left[1-\frac{\eta^2 a_p}{2}\frac{J_0(a_p)J_1(a_p)+Y_0(a_p)Y_1(a_p)}{J_1^2(a_p)+Y_1^2(a_p)}\right], \\ S_{r2}(a_p,\eta) = \frac{1}{\pi\left[J_1^2(a_p)+Y_1^2(a_p)\right]}. \end{cases} \tag{50}$$

In the above equation, $a_p = \omega R/c_p$ and $a_0 = \omega R/c_S$ are the dimensionless frequency for pressure and shear waves, respectively, while η denotes the ratio of the wave speeds:

$$\eta = c_P/c_S = \sqrt{2(1-\nu)/(1-2\nu)}. \tag{51}$$

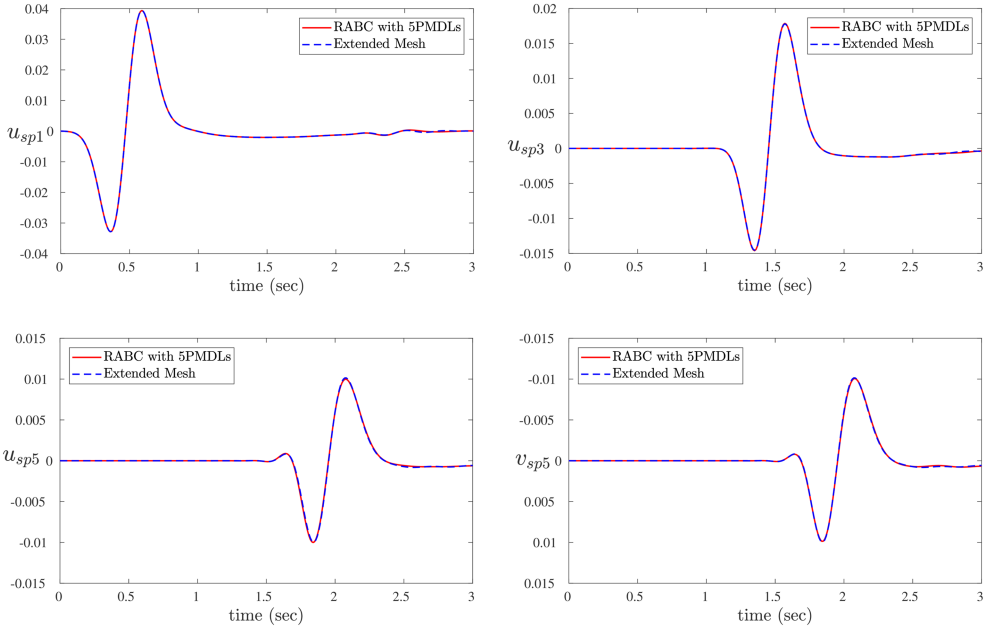

FIGURE 9 Radial response: time-history displacements at sample points [Colour figure can be viewed at wileyonlinelibrary.com]

TABLE 3 Radial response: Relative error at sample points between RABC-PMDLs and extended-mesh solutions

	u_{sp1}	v_{sp2}	u_{sp3}	v_{sp4}	u_{sp5}	v_{sp5}
Error	8.3232×10^{-3}	1.7350×10^{-2}	8.2235×10^{-3}	2.4342×10^{-2}	2.7395×10^{-2}	1.9242×10^{-2}

Abbreviations: PMDLs, perfectly matched discrete layers; RABC, reciprocal absorbing boundary condition.

We now apply a (radial) harmonic pressure $q(t) = \cos \omega t$ on the circle and let the response reach steady state. Three dimensionless frequencies $a_0 = 0.2\pi, \pi, 1.25\pi$ are chosen, representing ranges of low, medium, and high frequencies. At the highest frequency considered, $a_0 = 1.25\pi, f = 5Hz$, the mesh is shrunk by a factor of 4 so that it satisfies the requirement of having sufficient elements per minimum wavelength. In addition, the time-step size is smaller: $\Delta t = 0.0025$ s. Excellent agreement in terms of both amplitude and phase of the harmonic responses can be observed in Table 2.

5.3 | Torsional response

We proceed now to investigate the response in the circumferential direction. Specifically, the circle is now excited by a uniform tangential traction. The arrangement of RABC and PMDLs is the same as before. On the top edge, $y = 0$, the displacement in the x-direction must vanish, so the boundary condition $u(x, y) = 0$ is imposed. Similarly, on the left edge, $x = 0$, we specify the displacement $v(x, y) = 0$. Snapshots of the wave field can be seen in Figure 10. The response time histories at sample points are shown in Figure 11, while the corresponding relative errors are summarized in Table 4. From this table, we can see that the corner point $sp4$ has the highest relative error, which is around 1.8%, whereas the errors at points on the circle are very small, especially at $sp1$ (only 0.0225%).

The exact frequency-domain solution (dynamic torsional stiffness) is given by

$$S_\theta(a_0) = \frac{2\mu}{R}\left[1 - \frac{H_0^{(2)}(a_0)}{H_1^{(2)}(a_0)}\right] = \frac{2\mu}{R}\left[S_{\theta 1}(a_0) + iS_{\theta 2}(a_0)\right], \tag{52}$$

TABLE 4 Torsional response: Relative error at sample points between RABC-PMDLs and extended mesh solutions

	v_{sp1}	u_{sp2}	v_{sp3}	v_{sp4}
Error	2.2562×10^{-4}	2.7008×10^{-4}	3.9661×10^{-3}	1.8755×10^{-2}

Abbreviations: PMDLs, perfectly matched discrete layers; RABC, reciprocal absorbing boundary condition.

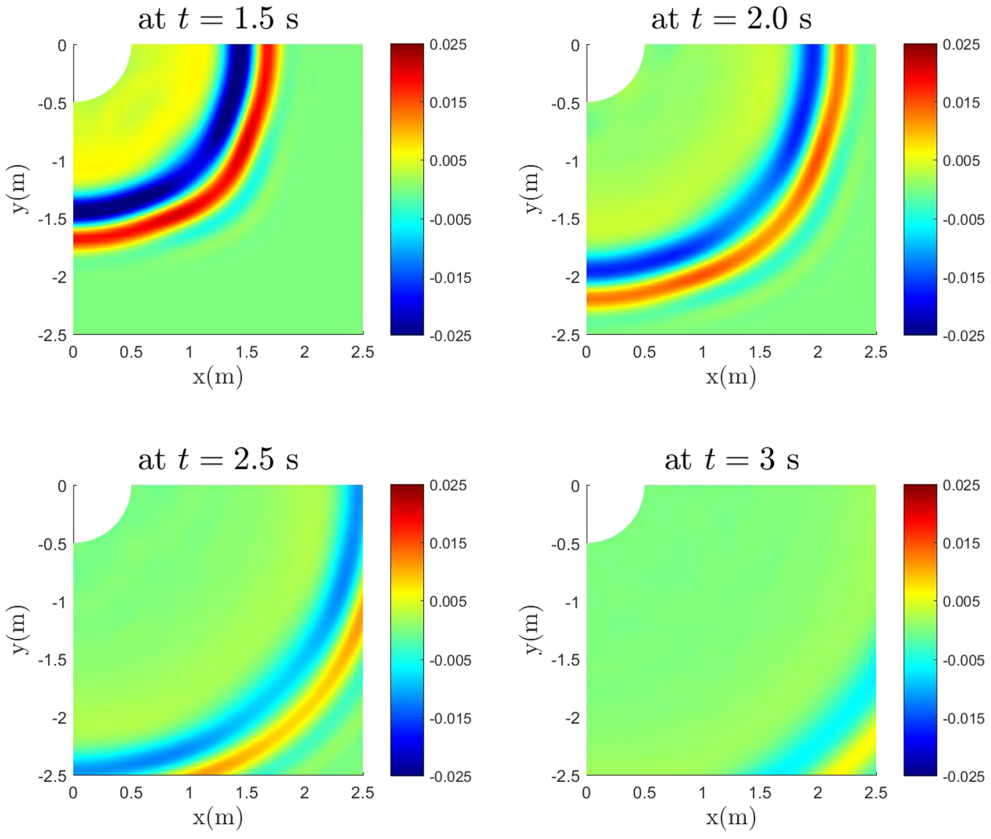

FIGURE 10 Torsional response: Snapshots of the wave field of the rotation u_θ/r at various times [Colour figure can be viewed at wileyonlinelibrary.com]

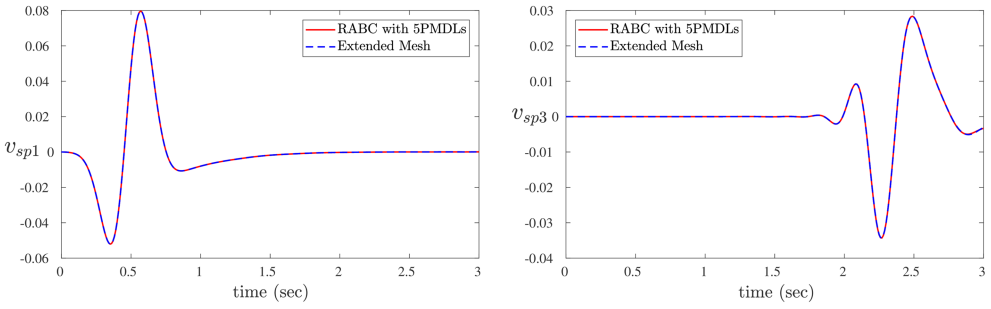

FIGURE 11 Torsional response: Displacement time histories at sample points [Colour figure can be viewed at wileyonlinelibrary.com]

where

$$\begin{cases} S_{\theta 1}(a_0) = 1 - \frac{a_0}{2}\frac{J_0(a_0)J_1(a_0)+Y_0(a_0)Y_1(a_0)}{J_1^2(a_0)+Y_1^2(a_0)}, \\ S_{\theta 2}(a_0) = \frac{1}{\pi[J_1^2(a_0)^2+Y_1^2(a_0)]}. \end{cases} \tag{53}$$

Again, the harmonic response is computed at three dimensionless frequencies $a_0 = 0.2\pi, \pi, 1.25\pi$. As shown in Table 2, the amplitude and phase of the solutions by RABC-PMDLs agree very well with the exact solution at all three frequencies.

5.4 | Horizontal response

Finally, we consider uniform horizontal traction on the circle. In this case, the Dirichlet boundary condition $v(x, y) = 0$ is specified on the edges $x = 0$ and $y = 0$. Snapshots of the horizontal wave field are shown in Figure 12. In the x-direction, the horizontal displacement u is in the direction of pressure-wave propagation (with speed c_p). In the y-direction, however, the displacement u is perpendicular to the direction of shear-wave propagation (with speed c_s). As we can observe in the snapshot at $t = 1$ s, the outermost red contour in the x-direction reaches the distance 1 m from the circle. However, the outermost red contour in the y-direction propagates to the point at only 0.5 m below the circle as, in this example, the

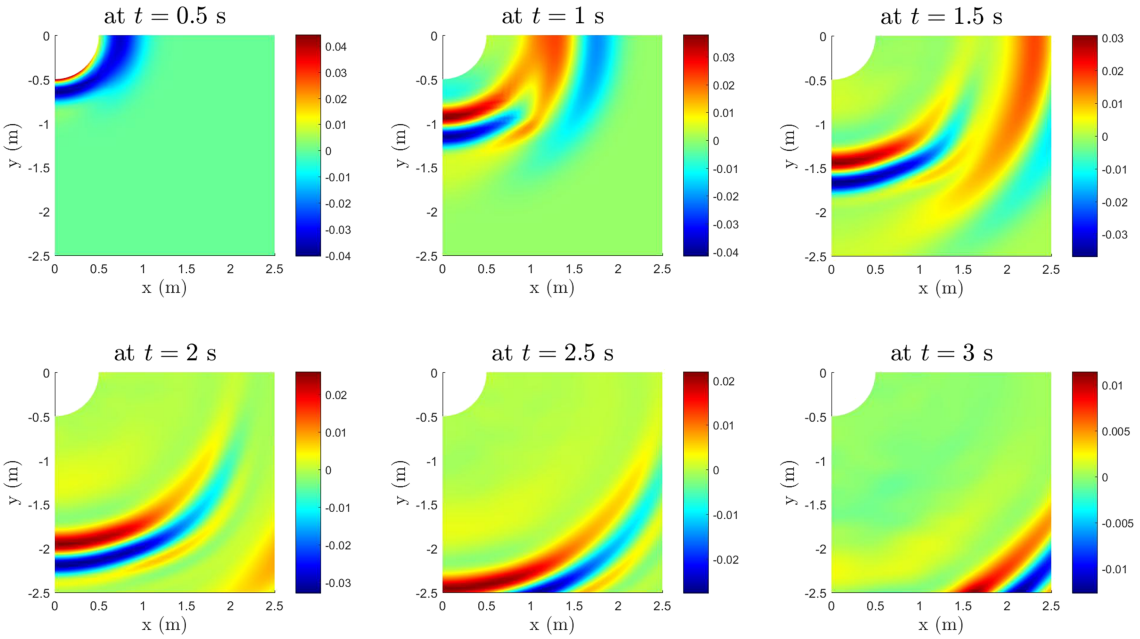

FIGURE 12 Horizontal response: Snapshots of the wave field of u at various times [Colour figure can be viewed at wileyonlinelibrary.com]

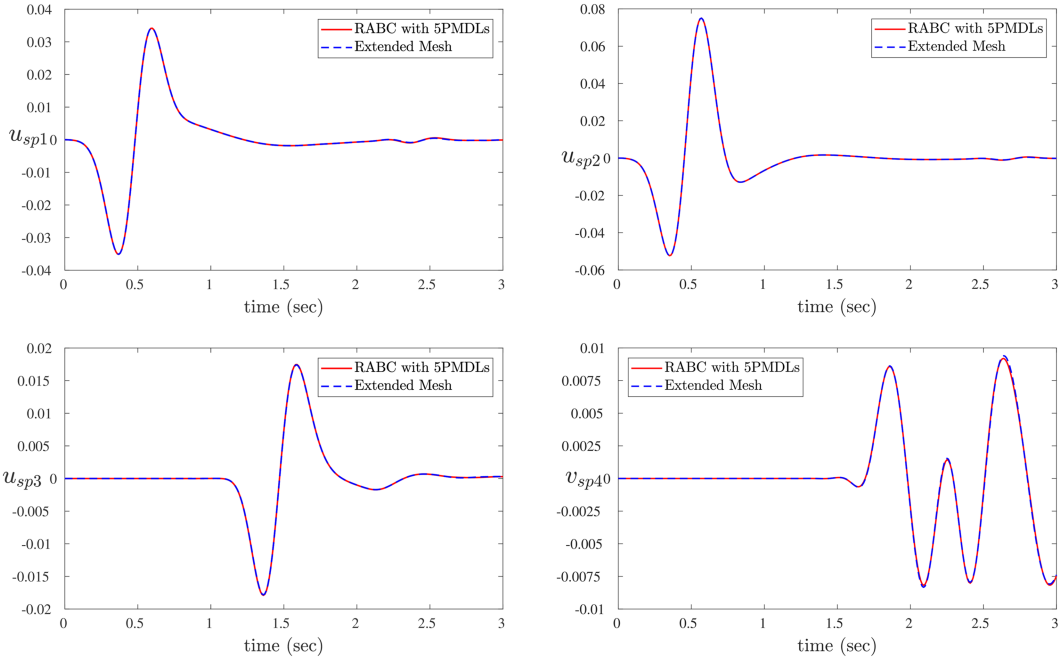

FIGURE 13 Horizontal response: Displacement time histories at sample points [Colour figure can be viewed at wileyonlinelibrary.com]

pressure-wave speed is twice the shear-wave speed ($c_p = 2c_s$). The observation here is also true for the snapshots at $t = 0.5$ s and $t = 1.5$ s. Response time-histories at sample points are plotted in Figure 13, and the relative errors are summarized in Table 5.

The exact frequency-domain solution for the dynamic horizontal stiffness can be written as

$$S_x(a_0) = -\pi\mu a_0^2 \frac{4K_1(a_p^*)K_1(a_0^*) + a_0^* K_1(a_p^*)K_0(a_0^*) + a_p^* K_0(a_p^*)K_1(a_0^*)}{a_p^* K_0(a_p^*)K_1(a_0^*) + a_0^* K_1(a_p^*)K_0(a_0^*) + a_p^* a_0^* K_0(a_p^*)K_0(a_0^*)}, \tag{54}$$

where $a_0^* = a_0 i$, $a_p^* = a_p i$, and $K_\nu(\cdot)$ is the *modified* Bessel function of the second kind ($\nu = 0, 1$).

	u_{sp1}	u_{sp2}	u_{sp3}	v_{sp4}
Error	3.5556×10^{-3}	2.0769×10^{-3}	5.3087×10^{-3}	2.0250×10^{-2}

Abbreviations: PMDLs, perfectly matched discrete layers; RABC, reciprocal absorbing boundary condition.

TABLE 5 Horizontal response: Relative error at sample points between RABC-PMDLs and extended mesh solutions

Table 2 summarizes the amplitudes and phases of the computed (time-domain) steady-state amplitudes and phases in comparison with exact frequency-domain results at the three frequencies considered in all numerical examples. Excellent agreement can be seen even in this most demanding case of horizontal excitation that involves both shear and pressure waves.

6 | CONCLUSIONS

We have presented an application of a RABC with PMDLs to problems of wave motion due to excitations of a circular disk in full space. Specifically, four cases were considered, namely, vertical (axial), radial, torsional, and horizontal vibrations. Numerical examples shown in this paper demonstrate that RABC-PMDLs coupling yields accurate solutions. The combination proposed herein is amenable to extension in three dimensions, a topic of future research on reciprocal absorbing boundaries.

ORCID

Cuong T. Nguyen https://orcid.org/0000-0002-9948-5639

REFERENCES

1. Brebbia CA, Dominguez J. Boundary element methods for potential problems. *Appl Math Model*. 1977;1(7):372–378.
2. Tassoulas JL, Kausel E. On the dynamic stiffness of circular ring footings on an elastic stratum. *International journal for numerical and analytical methods in geomechanics*. 1984;8(5):411–426.
3. Waas G. Linear two-dimensional analysis of soil dynamics problems in semi-infinite layered media. *Dissertation presented to the University of California at Berkeley*. 1972.
4. Kausel E. Forced vibrations of circular foundations on layered media. M.I.T. Research Report R74-11, Soil publication, Structures publication.
5. Engquist B, Majda A.. Absorbing boundary conditions for numerical simulation of waves. *Proc Natl Acad Sci*. 1977;74(5):1765–1766.
6. Higdon RL. Numerical absorbing boundary conditions for the wave equation. *Mathematics of computation*. 1987;49(179):65–90.
7. Kausel E, Tassoulas JL. Transmitting boundaries: a closed-form comparison. *Bull Seismol Soc Am*. 1981;71(1):143–159.
8. Guddati MN, Tassoulas JL. Continued-fraction absorbing boundary conditions for the wave equation. *J Comput Acoust*. 2000;8(1):139–156.
9. Israeli M, Orszag CA. Approximation of radiation boundary conditions. *Journal of computational physics*. 1981;41(1):115–135.
10. Berenger JP. A perfectly matched layer for the absorption of electromagnetic waves. *Journal of computational physics*. 1994;114(2):185–200.
11. Guddati MN, Lim KW. Continued fraction absorbing boundary conditions for convex polygonal domains. *Int J Numer Methods Eng*. 2006;66(6):949–977.
12. Basu U, Chopra AK. Perfectly matched layers for time-harmonic elastodynamics of unbounded domains: theory and finite-element implementation. *Comput Methods Appl Mech Eng*. 2003;192(11-12):1337–1375.
13. Nguyen CT, Tassoulas JL. Reciprocal absorbing boundary condition for the time-domain numerical analysis of wave motion in unbounded layered media. In: Proceedings of the Royal Society A:Mathematical, Physical and Engineering Sciences, Vol. 470; 2017.
14. Nguyen CT, Tassoulas JL. Reciprocal absorbing boundary condition with perfectly matched discrete layers for the time-domain propagation of SH waves in a layered half-space. *Soil Dyn Earthq Eng*. 2017;99:44–55.
15. Nguyen CT, Tassoulas JL. Reciprocal absorbing boundary condition with perfectly matched discrete layers for transient analysis of SV-P waves in a layered half-space. *Int J Solids Struct*. 2018;155:89–108.
16. Achenbach JD. Reciprocity and related topics in elastodynamics. *Appl Mech Rev*. 2006;59(1):13–32.
17. Hughes TJ. The finite element method: linear static and dynamic finite element analysis. *Courier Corporation*. 2012.
18. Guddati M. N.. Arbitrarily wide-angle wave equations for complex media. *Comput. Methods Appl. Mech. Eng.* 2006;195(1):949–977.
19. Baranov VA. On the calculation of an embedded foundation (in Russian); 1967:195–209.
20. Novak M. Dynamic stiffness and damping of piles. *Can Geotech J*. 1974;11(4):574–598.
21. Meza-Fajardo KC, Papageorgiou AS. A nonconvolutional, split-field, perfectly matched layer for wave propagation in isotropic and anisotropic elastic media: stability analysis. *Bulletin of the Seismological Society of Americ*. 2008;98(4):1811–1836.

22. Semblat J-F, Lenti L, Gandomzadeh A. A simple multi-directional absorbing layer method to simulate elastic wave propagation in unbounded domains. *Int J Numer Methods Eng*. 2011;85(12):1543–1563.
23. Liu G, Jerry SQ. A non-reflecting boundary for analyzing wave propagation using the finite element method. *Finite Elem Anal Des*. 2003;39(5-6):403–417.
24. Nguyen CT, Tassoulas JL. Application of reciprocal absorbing boundary condition to transient analysis of acoustic wave propagation. *Comput Methods Appl Mech Eng*. 2018;329:55–74.

How to cite this article: Nguyen CT, Tassoulas JL. Transient analysis of full-space unbounded domains by reciprocal absorbing boundaries. *Int J Numer Anal Methods Geomech*. 2020;44:3–18. https://doi.org/10.1002/nag.2987